Advanced Physics Research

ADVANCED PHYSICS RESEARCH Open Access

www.advphysicsres.com

RESEARCH ARTICLE OPEN ACCESS

Ultrafast Control of Coherent Acoustic Lattice Dynamics in the Transition Metal Dichalcogenide Alloy WSSe

Sergio I. Rey[1] | Martin J. Cross[1] | Malte L. Welsch[1] | Frederik Schröder[1,2] | William V. Carstensen[1] | Oleg Semyonov[3] | Daphne M. Dekker[3] | Nikolai Orlov[3] | Binbin Zhou[1] | Nicolas Stenger[1,2] | Peter U. Jepsen[1] | Edmund J. R. Kelleher[1]

[1]DTU Electro, Technical University of Denmark, Kgs. Lyngby, Denmark | [2]NanoPhoton–Center for Nanophotonics, Technical University of Denmark, Kgs. Lyngby, Denmark | [3]AMOLF, Amsterdam, Netherlands

Correspondence: Sergio I. Rey (s.reypuentes@amolf.nl) | Edmund J. R. Kelleher (edkel@dtu.dk)

Received: 30 June 2025 | **Revised:** 30 December 2025 | **Accepted:** 9 February 2026

ABSTRACT

Coherent acoustic phonons (CAPs)—-vibrational modes prepared in a coherent state that propagate as long-wavelength strain waves—can dynamically modulate crystal structure and, in some cases, symmetry, offering unique opportunities for controlling material properties. We investigate CAP generation in exfoliated multilayer flakes of the alloy tungsten sulfide selenide ($WS_{2x}Se_{2(1-x)}$, hereafter WSSe). Using high-fluence 400 nm excitation together with ultrafast transient-reflection spectroscopy, we track the coupled carrier-lattice response, revealing dynamics consistent with a sequence of rapid carrier thermalization and exciton formation, phonon recycling, and photoinduced stress from prompt deformation potential and slower thermoelastic contributions that combined drive a coherent oscillation at 27 GHz. The fractional amplitude of the oscillatory component attributed to an acoustic mode in a coherent state is substantially larger in WSSe than in the parent crystals WS_2 and WSe_2, where the coherent contribution represents only a minor perturbation superimposed on a dominant monotonic background. This pronounced enhancement indicates that the alloy does not behave as a simple interpolation between the binary compounds, but instead exhibits an emergent optical-acoustic response linked to chalcogen mixing. Finally, by implementing a two-pulse excitation scheme, we demonstrate optical control of the CAP phase and amplitude, highlighting the potential of TMDC alloys to support dynamic modulation of optomechanical and acoustic responses for advanced device engineering.

1 | Introduction

Van der Waals materials offer a promising platform for the development of future photonic, optoelectronic, and hybrid devices owing to their chemical tunability, potential for reduced dimensionality, and weak inter-layer coupling leading to diverse optical, electrical and thermal properties [1–7]. Among them, transition metal dichalcogenides (TMDCs) have attracted particular attention. Their bandgap energies evolve strongly with thickness [8], monolayer forms exhibit high photoluminescence efficiency [9], and the valley degree of freedom can be selectively addressed using circularly polarized light [10, 11]. The properties and behavior of TMDCs can be modified by introducing asymmetry in their chalcogen coordination. Janus TMDCs, structures where the two faces of the monolayer are terminated by different chalcogen species (e.g., S-W-Se), break inversion symmetry and possess additional properties, including an intrinsic piezoelectricity [12] and, in some cases, extended carrier lifetimes [13]. However, the controlled synthesis of Janus monolayers remains experimentally challenging [14, 15]. Substitutional chalcogen alloys, with general chemical formula $MA_{2x}B_{2(1-x)}$ (M = Mo, W, and A, B = S, Se, and Te), offer an alternative route that permits continuous band gap tuning and can host distinct optical states, including dark excitons and trions [16]. These alloys also possess reduced

out-of-plane symmetry compared to their pure counterparts, and first-principles calculations show that the local S/Se/Te asymmetry can generate a weak, spatially varying out-of-plane dipole field that may modulate the optical and acoustic response of the material [17]. Our objective here is to examine how this alloying-induced asymmetry in multi-layer bulk-like WSSe flakes reshapes the ultrafast transient reflection response compared to the binary endpoint compounds.

Central to fully harnessing the potential of TMDCs is the ability to control their structural degrees of freedom. Activating coherent phonons as collective excitations can trigger phase transitions that dramatically alter materials properties [18]. In particular, using light waves to control such transitions offers promising avenues for future logic device architectures [19]. Coherent acoustic phonons (CAPs), which propagate as strain waves, are useful for probing phonon-electron, phonon-plasmon, and phonon-magnon interactions [20–22]. Using ultra-short pulsed laser sources, the generation and control of GHz-THz phonon vibrations have been extensively explored [23–26]. In TMDCs, coherent phonons have been observed in several crystal compounds, including MoS_2 [27], $PtSe_2$ [28], $PdSe_2$ [29], and in InSe/hBN heterostructures [30]. Furthermore, strain induced in layered topological insulators like Bi_2Se_3 can access novel topological phases [31, 32].

In this work, we investigate the ultrafast dynamics of bulk WSSe using single- and double-pump-probe spectroscopy in reflection geometry. Our observations can be rationalized within a multi-step mechanism involving rapid exciton formation, phonon recycling, and subsequent laser-induced heating, which together launch a propagating strain wave via carrier-induced and thermoelastic stress contributions. Notably, the fractional amplitude of the coherent oscillation in WSSe is substantially larger than in the symmetric parent compounds WS_2 and WSe_2. Such an enhanced response in the alloy is compatible with the presence of a weak built-in out-of-plane dipole field arising from the chalcogen asymmetry. A phenomenon established in few-layer alloys [33], although additional measurements are needed to confirm its manifestations in thick, bulk-like flakes. If present, this asymmetry-driven mechanism may be found in other TMDC alloys with reduced out-of-plane symmetry, suggesting opportunities for engineering new optomechanical functionalities.

2 | Experimental Methods

2.1 | Sample Preparation

High-quality TMDC crystals—WS_2 and WSSe (HQ Graphene) and WSe_2 (2D semiconductors)—were studied. All crystals were synthesized by chemical vapor transport (CVT). Vendor-provided energy-dispersive X-ray (EDX) analysis of the WSSe crystal indicated an average chalcogen composition of approximately 29.8% S and 37.0% Se.

The crystals were mechanically exfoliated using the Scotch-tape method (3M High-Performance Double Coated Tape 9087). The adhesive side was used for exfoliation, while the tape's backing was secured to a microscope slide to provide mechanical support and to expose a fresh (001)-oriented surface for reflection-mode measurements carried out under vacuum. Optical-contrast microscopy and atomic-force measurements of the surface topography indicate exfoliated flake thicknesses of several hundred nanometers, implying bulk-like optical and vibrational behavior.

All samples crystallize in the 2H phase. Electron backscatter diffraction (EBSD), Raman spectroscopy, and X-ray diffraction (XRD) measurements revealed no evidence of secondary phases, stacking faults or surface degradation (see Supporting Information).

2.2 | Single- and Double-Pump-Probe Spectroscopy

Our experimental setup employed a Ti:Sapphire regenerative amplifier (Solstice Ace, Spectra Physics) that generated ∼100 fs pulses centered at 800 nm with a 1 kHz repetition rate. The laser output was split into three segments: two equally intense beams serve as pump pulses, while a significantly attenuated beam was used as the probe. To optimize the signal-to-noise ratio, the probe path remains fixed, whereas the relative timing of the pump pulses was adjusted using mechanical delay stages. Both pump beams were frequency-doubled in β-barium borate (BBO) crystals, converting them to 400 nm pulses, while the probe remains at the original 800 nm wavelength. Figure 1a schematically depicts the simplified experimental layout and detection configuration. Both pump pulses and the probe pulse impinge on the crystal at normal incidence. At time $t = 0$, as shown in the inset, the pump beam generates a strain pulse (i.e., a coherent acoustic phonon, or CAP) on the surface of the WSSe sample. The probe is subsequently reflected by the strain pulse—that propagates at the longitudinal speed of sound, v_s—and by the crystal surface.

A homodyne detection scheme is applied using a reference frequency of 500 Hz supplied by an optical chopper. The reflected probe signal is measured with a balanced photodiode and sequentially processed through a boxcar integrator and lock-in amplifier synchronized to the chopper frequency. For double-pulse experiments, the chopper is strategically placed in the shared optical path of both pump beams, ensuring that the lock-in amplifier simultaneously captures signals originating from the influence of both pump pulses.

3 | Activation of a Coherent Acoustic Oscillation in WSSe

Figure 1b illustrates the sequence of photophysical processes initiated by high-fluence excitation with 400 nm pump photons, ultimately leading to the generation of a coherent acoustic phonon. The transient reflection data in Figure 1c, recorded at an excitation fluence of $F \sim 5$ mJ cm^{-2}, reveals these dynamics in detail. Initially, a single pump pulse excites carriers to high-energy states in the conduction band, driving the system out of equilibrium and producing a corresponding increase in the transient reflectivity. These photoexcited carriers rapidly thermalize to the bottom of the conduction band via electron-electron and electron-phonon scattering, exhibiting a single-exponential decay (black curve) with a time constant of $\tau_{el} = 369$ fs, as shown in Figure 1c. In addi-

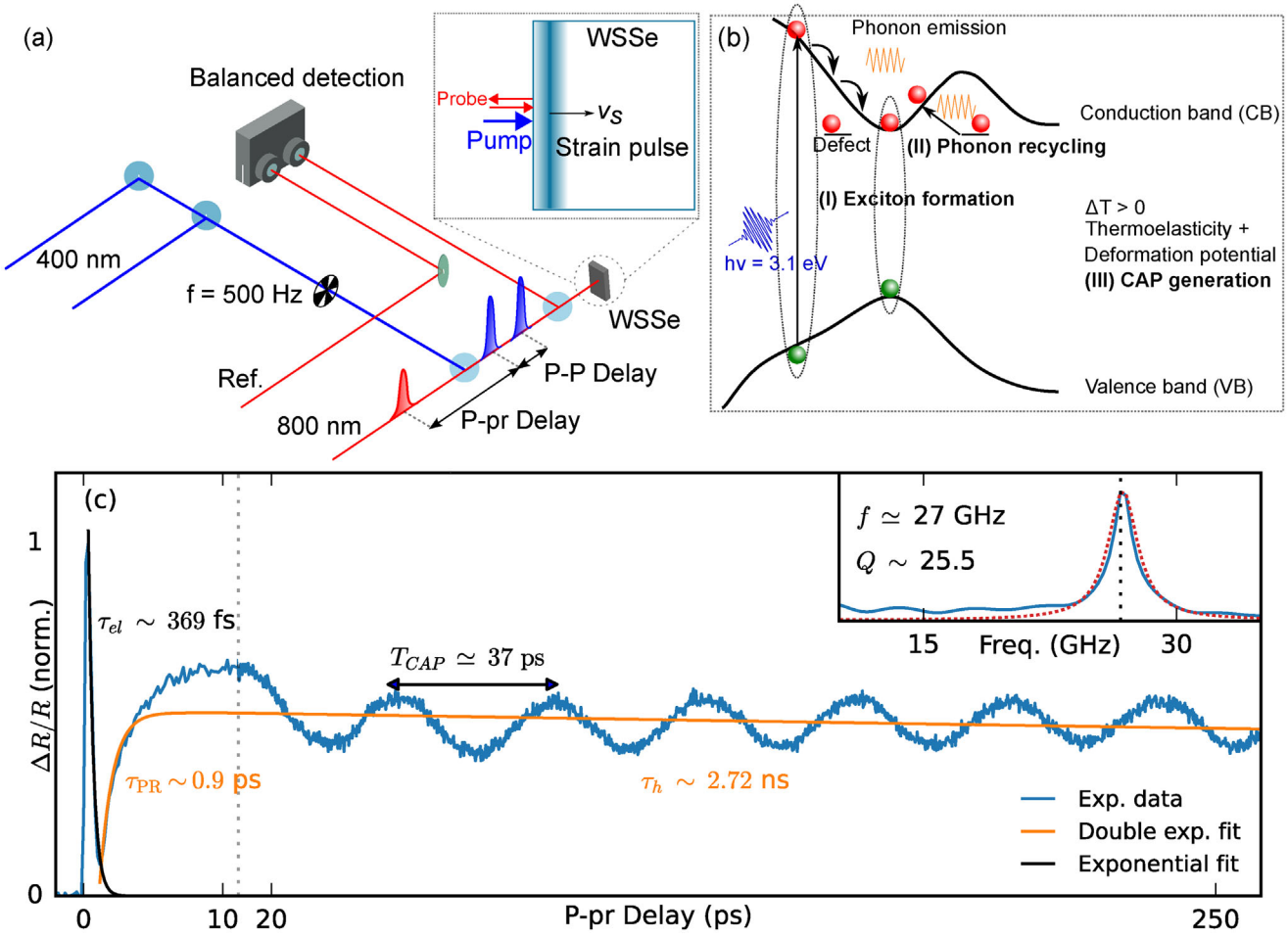

FIGURE 1 | Ultrafast spectroscopy of WSSe. (a) Experimental setup. A Ti:Sapphire amplifier at 800 nm generates 100 fs pulses and is split into three arms. A weak probe and two pump pulses at 400 nm, generated by SHG in a BBO crystal, which are modulated using an optical chopper at 500 Hz. For double-pump excitation, the pump-pump (P-P) delay is kept constant. Inset: The propagating photoinduced strain pulse reflects the probe light. (b) Schematic of the photophysical processes in WSSe upon above-gap photoexcitation. (I) Thermalization and exciton formation. (II) Phonon recycling and (III) CAP generation via the deformation potential and thermoelastic mechanisms. (c) Transient reflection of WSSe. The time domain dynamics exhibit the multiple processes after photoexcitation: namely, exciton formation and thermalization, followed by a recovery of the signal caused by the phonon recycling effect, preceding the emergence of a periodic modulation due to the generation of a CAP. (d) The Fourier spectrum (blue) and its Lorentzian fit (red dots). The spectrum peaks at ≃ 27 GHz and has a quality factor of $Q \sim 25.5$.

tion to carrier thermalization, other competing processes occur on similar timescales. For example, Valencia-Acuña et al. [34] demonstrated that exciton formation predominantly contributes to the fast decay in TMDC monolayers, using a photodope-pump-probe scheme with similar wavelengths. This interpretation is further supported by the pump photon energy of 3.1 eV, which can quasi-resonantly excite the D-exciton resonance, known to be present in both WS_2 [35] and Janus monolayers of WSSe [13]. Similarly, other semiconductors such as GaAs [36] and the ternary TMDC alloy, MoWSe, [37] exhibit nonradiative trapping within the first picosecond following photoexcitation. At this high fluence, carrier thermalization, exciton formation, and nonradiative trapping likely compete, as not all free carriers can bind into excitons [38–41].

The transient reflection signal fully decays within 1 ps and subsequently recovers over the remainder of the experimental delay range. We fit the subsequent rise and decay of the transient reflection with a double-exponential model, highlighted by the orange line. The rising component has a time constant of τ_r = 950 fs and is attributed to the phonon recycling (PR) mechanism. In this process, free carriers thermalize to the bottom of the conduction band while emitting phonons that result in an increased lattice temperature [37]. These incoherently generated phonons can transfer energy to carriers trapped in midgap states, repopulating the conduction band. This effect has been observed across various systems—including symmetric alloys ($MoWS_2$), asymmetric alloys (MoSSe and WSSe), and binary TMDCs (MoS_2, WS_2) [37]—and is analogous to the mechanism reported in graphene-WS_2 heterostructures, where acoustic phonon energy is transferred from graphene to WS_2 [42]. The slower decay component, characterized by a time constant of τ_h = 2.72 ns, is ascribed to heat dissipation via thermal diffusion. Similar nanosecond-scale decay times due to thermal diffusion have been observed in WTe_2 [43] and other multilayered semiconductors [44], under comparable pump-probe conditions. While various long-lived processes, such as phonon bottlenecks [45], intervalley exciton scattering [46], defect-bound excitons [47],

and Auger recombination [48] have been reported in TMDC monolayers, none extend into the nanosecond regime.

The CAP manifests as a periodic modulation superimposed on the slower exponential decay of the transient reflection signal. After subtracting the double-exponential background and applying a fast Fourier transform (FFT), we observe a prominent oscillation at approximately 27 GHz (see the power spectrum in the inset of Figure 1c), corresponding to a period of $T_{CAP} = 37$ ps. This modulation arises from the constructive and destructive interference between the probe light reflected from the crystal surface and that reflected from the propagating CAP—a process discussed further in Section 4. We attribute the observed longitudinal CAP to photoinduced stress that contains a prompt carrier-induced component commonly described by deformation potential (DP) coupling. In this picture, changes in carrier occupation generate an electronic stress through the strain dependence of band energies, launching a coherent longitudinal stain wave [49]. We rule out the possibility of transverse CAP generation, as such modes cannot be detected when both the pump and probe beams impinge on the sample at normal incidence [50].

The DP mechanism is widely regarded as the primary source of CAP generation in semiconductors. Although thermoelastic stress can become increasingly important at high fluences [49, 51], we argue that under our experimental conditions—characterized by high-energy photon excitation—the initial CAP generation is dominated by carrier-induced DP stress. This interpretation is supported by the long carrier lifetime (nanosecond scale), allowing carrier-induced stress to persist on timescales comparable to or exceeding multiple CAP oscillation periods [52]. Moreover, lattice heating associated with carrier thermalization primarily modifies carrier trapping and repopulation pathways (the PR channel), while the CAP launch remains primarily governed by photoinduced stress. In this regime, re-excitation of trapped carriers via PR can transfer energy back to the electronic system, depleting the incoherent phonon population through reabsorption [37].

The quality factor Q serves as a key figure of merit for comparing oscillatory systems [30, 53]. It is defined as the ratio of the oscillation frequency relative to the spectral width of the oscillation (related to the oscillation lifetime in the time-domain): $Q = f/\Delta f$. Due to limitations in our experimental delay range, we approximate the lifetime by fitting the oscillatory component with a decaying cosine function of the form $A\exp(-t/\tau_{osc})\cos(2\pi f t + \phi)$, where the decay constant, $\tau_{osc} = 355$ ps. We then extend the time axis based on this decay constant and calculate the FFT, as shown in the inset of Figure 1c. By fitting a Lorentzian profile to the Fourier peak, we extract the spectral width Δf and thus estimate Q. Our analysis yields $Q \sim 25.5$. While this value is lower than the highest Q reported in optomechanical and nanophononic platforms [53], it is notably higher than the quality factors observed in hBN [30] and acoustoplasmonic nanocrosses [21].

We can vary the thermoelastic contribution to the coherent oscillation by increasing the pump fluence. Figure 2a compares transient reflection signals at two different fluences, normalized to the sharp peak at zero delay (indicated by the horizontal dotted black line). At a fluence of $F \sim 10.4$ mJ cm^{-2}, the recovered signal exceeds the initial peak. Such behavior cannot be explained solely by the PR mechanism—even at 100% efficiency, re-exciting all trapped carriers would produce a recovered signal no greater than the original peak, given that its magnitude is proportional to the number of photoexcited carriers. Therefore, we infer that the amplitude of the coherent oscillation increases with fluence because thermoelastic deformation becomes more dominant. Figure 2b shows the power spectra of the oscillatory component after subtracting the non-oscillatory background. Although no frequency shift is observed with increasing fluence, the amplitude of the CAP increases linearly, as shown in Figure 2c with orange diamonds, with no detectable sign of saturation. The increasing oscillation amplitude with fluence indicates an increasing contribution from lattice heating and thermoelastic stress, consistent with expectations for photoinduced thermal expansion at high excitation densities [27, 51].

We show the evolution of the rising and decaying exponential components as a function of fluence in Figure 3a,b, respectively. The fast rise time, attributed to the PR mechanism, remains nearly fluence independent, implying that the underlying dynamics are associated with an intrinsic phonon timescale. This observation is consistent with previous studies [37]. In contrast, the slow component—extracted from double-exponential fitting—initially increases with fluence, indicating a reduced effective heat dissipation rate at higher excitation densities. For fluences above 5 mJ cm^{-2}, the extracted time constant decreases, which may reflect enhanced phonon-phonon scattering at elevated phonon populations [37, 54, 55]. The data point at ~ 8 mJcm^{-2} deviates from the overall trend and may be influenced by the sensitivity of the fit due to the limited temporal scan range of the measurements. Finally, we note that there was no measurable change in the fast decay constant τ_{el}, supporting the assignment of exciton formation as the dominant process at short delay times [34].

4 | Comparison with WS_2 and WSe_2

To elucidate the influence of crystal asymmetry on the transient reflection dynamics, we compared the responses of symmetric TMDCs with that of the alloy WSSe. Figure 4a–c display the normalized transient reflection signals for WS_2, WSSe, and WSe_2, respectively, under similar experimental conditions. The transient reflection dynamics of both parent TMDCs show a negative behavior shortly after photoexcitation. In semiconducting materials, this is typically attributed to photoinduced absorption, as additional states created by the pump pulse become available in the conduction band. In WS_2, the transient reflection characteristics are well described by a double exponential function, where the fast component reflects rapid thermalization (and potentially exciton formation) [34, 38], while the slower component corresponds to carrier recombination processes [36]. Notably, the sign of the transient reflection signal is inverted after a characteristic delay—approximately 35 ps for WS_2 and 10 ps for WSe_2. This inversion is likely a result of renormalization of the bandgap, where a high density of electrons induces a change in the gap energy [35, 36, 56, 57]. The differences in inversion times may be linked to their distinct bandgaps—about 1.2 eV for bulk WS_2 and 1.35 eV for WSe_2 [58, 59]—as well as other factors that

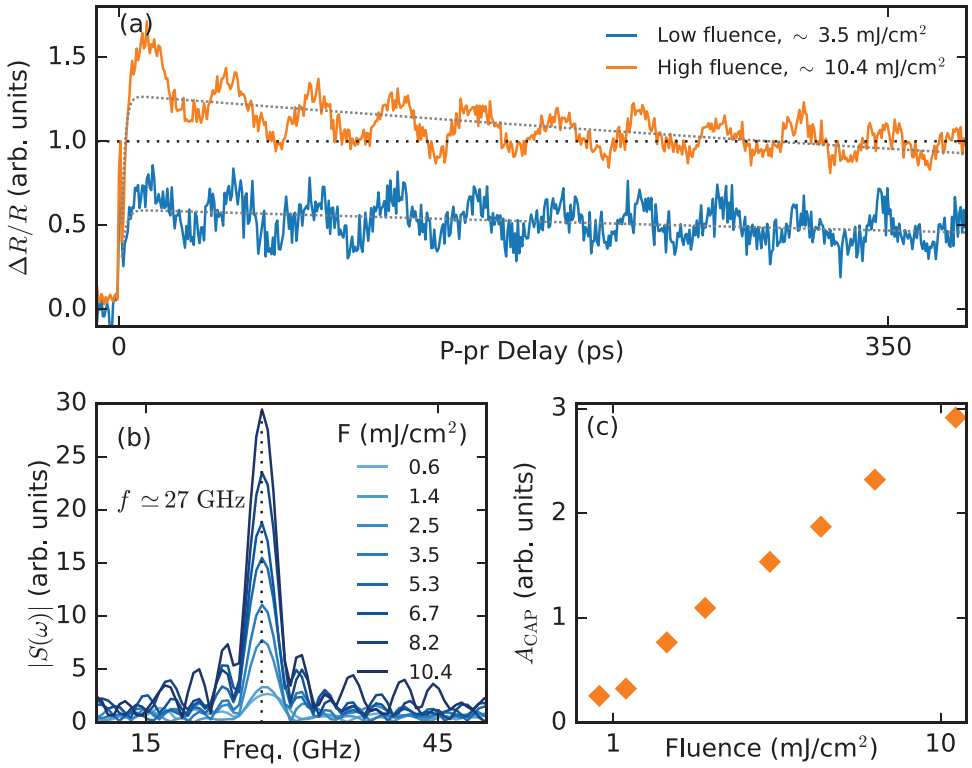

FIGURE 2 | Fluence dependence of CAPs. (a) Comparison between the low- and high-fluence excitation. The curves are normalized to the exciton formation peak at short delays. For the high-fluence regime, we see that the recovered signal after the phonon recycling effect surpasses the amplitude of the peak (black dotted line). In grey, the double-exponential fits of the signal for long delays. (b) Fourier spectra as a function of fluence. The peak at 27 GHz does not exhibit a frequency shift, but the amplitude increases monotonically with fluence. (c) Amplitude of the CAP versus fluence. The peak amplitude increases linearly with fluence.

TABLE 1 | Frequency and quality factor of the CAP in the three TMDC crystals studied.

TMDC	f (GHz)	Q
WS_2	28.2	4.9
WSe_2	29.4	1.4
WSSe	26.9	25.5

require more detailed microscopic modeling. Additionally, the WSe_2 signal exhibits an extra rapid increase in $\Delta R/R$ immediately after the arrival of the pump pulse, commonly attributed to a hole-filling effect observed in some semiconductors [52].

The transient reflection signals of all three materials display periodic modulation superimposed onto the overall response; notably, however, the amplitude of the oscillatory component in WSSe is significantly larger than in the symmetric TMDCs. Figure 4d shows the power spectra of the normalized signals after subtraction of the non-oscillatory background. Background removal can introduce artifacts in the low frequency region ($\lesssim 10$ GHz) [30], and thus we have omitted this portion of the spectrum for clarity. Table 1 summarizes the oscillation frequencies and the quality factors, Q, for the three TMDCs, determined using the method described in Section 3.

Analysis of the Fourier spectra and the corresponding quality factors clearly indicates that the CAP activated in the WSSe alloy exhibits both a larger fractional amplitude and a longer lifetime than is observed in the symmetric parent TMDCs. This distinct behavior suggests that the acoustic phonon dynamics in the alloy are not simply intermediate between those of the WS_2 and WSe_2, but reflect intrinsic features of the mixed-chalcogen lattice. One potential contributor to the enhanced oscillatory response is local S/Se asymmetry, which in few-layer alloys has been associated with weak out-of plane dipoles, although its presence in bulk remains uncertain. Substitution of sulfur with selenium disrupts the layer-wise inversion symmetry of the crystal, thereby producing a local out-of-plane dipole that behaves as a piezoelectric field under mechanical strain [60]. From a thermodynamic perspective, the induced lattice distortion—caused by the replacement atom—increases the configurational entropy of the material [61], which has been suggested to enhance piezoelectric properties [62]. Related mechanisms have been demonstrated in alloyed nitrides [63, 64], in ternary TMDC alloys [65], and have been predicted for MXY alloys [66] as well as in perfectly asymmetric Janus monolayers [12]. Of particular relevance, Nayak et al. [33], showed that TMDC alloys with an even number of layers exhibit a piezoelectric response, and that it can increase with the number of layers. Additionally, strong electron–phonon interactions in piezoelectric resonators can markedly reduce energy loss mechanisms [67], which may contribute to the superior figure of merit of the WSSe alloy observed in our experiments. However, in the bulk limit the

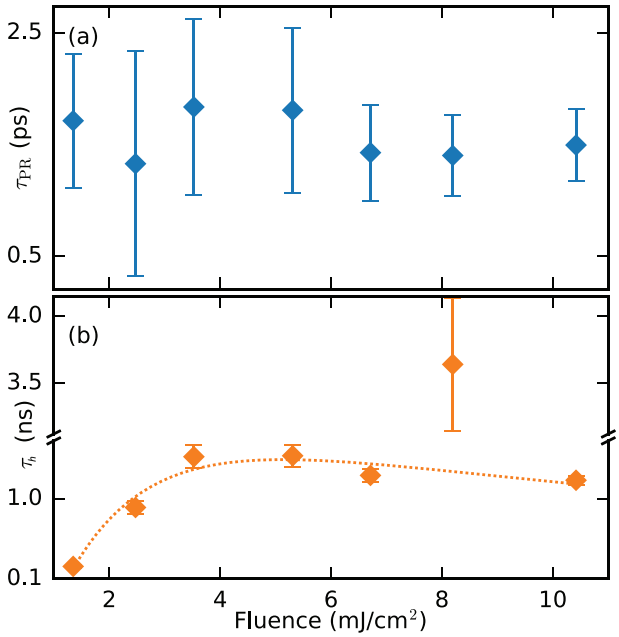

FIGURE 3 | Characteristic time constants in WSSe. Constant τ_{PR} as a function of fluence (a) and double-exponential behavior of τ_h, fitted with orange dotted line (b).

random distribution of chalcogen sites is expected to average the macroscopic dipole field toward zero, making it unlikely that a uniform built-in polarization accounts fully for the enhanced fractional amplitude of the CAP in WSSe. Further measurements (such as piezo-response force microscopy) are necessary to conclude whether alloy-induced asymmetry plays a direct role in the large oscillatory component of the transient reflectivity.

To describe the CAP, we adopt the framework proposed by Liu et al. in reference [68] for propagating strain pulses in GaN/InGaN heterostructures. In our case, this model is used as a phenomenological description of the optical interference between the probe reflected from the surface and from the propagating strained region. Its use here does not assume, nor rely upon, the large built-in piezoelectric fields characteristic of nitride-based heterostructures. Given our photoexcitation and detection geometries, we assume that only longitudinal strain pulses are activated—thus, only the out-of-plane elastic constant, C_{33}, is required. A schematic of the macroscopic model is shown in Figure 4e. The photoinduced strain pulse is represented as a thin, uniformly strained layer in the sample, where the refractive index n' deviates slightly from that of the unstrained material, n. This strained layer is located at a depth $z = v_s\tau$, where τ denotes the pump-probe delay, and its thickness d is treated as a phenomenological parameter corresponding to the spatial extent of the CAP wavepacket. The speed of sound v_s is given by [68]:

$$v_s = \sqrt{C_{33}/\rho} \tag{1}$$

where ρ is the mass density. We further assume that the modified refractive index remains constant within the strained region, i.e., for $z \in [z, z+d]$. The transient reflection signal is then calculated by summing the dominant first three terms of the Fabry-Perot series, $r = r_0 + r_1 + r_2$, yielding [68]:

$$\frac{\Delta R}{R}(\omega, t) \propto |\delta n| \sin(kd) \sin\left(2\pi \frac{t}{T} + \phi\right) \tag{2}$$

where ϕ is the phase of the CAP and k the magnitude of the wavevector. The oscillation period, T, is given by the relation [24, 69]:

$$T = 1/f = \frac{\lambda}{2v_s n} \tag{3}$$

with λ denoting the probe wavelength. A key outcome of this model is that the amplitude of the coherent oscillation depends exclusively on the change in the refractive index and the thickness of the strained layer, while the oscillation frequency is determined by the longitudinal speed of sound and the refractive index at the probing wavelength.

Due to the absence of experimental measurements for the optical constants of WSSe alloys, we estimate its refractive index at 800 nm using Equation (3). First, we calculate the speed of sound from Equation (1). To do so, we approximate the mass density by combining the known sulfur-to-selenium ratio in the alloy with the reported densities of WS_2 [70] and WSe_2 [71].

We use the out-of-plane elastic constant $C_{33} = 5.53 \times 10^{10}$ Pa obtained from density functional theory (DFT) simulations of an ideal Janus WSSe monolayer [12], as neither experimental measurements nor bulk-specific values for WSSe are currently available. We therefore apply this elastic constant as an approximate reference, noting that the exact effective C_{33} in bulk WSSe flakes may differ. With these parameters, the speed of sound is calculated as $v_s = \sqrt{C_{33}/\rho} = 2618.2$ m s^{-1}, which, when applied to Equation (3) yields a refractive index of $n = 4.09$. Figure 4f compares our calculated refractive index for WSSe with experimental values for the parent TMDCs. The x-axis shows the longitudinal speed of sound for bulk WSe_2 (orange) and WS_2 (blue), as determined by Muratore et al. [72]. The y-axis displays refractive indices measured for three-layer samples by Hsu et al. [73] (circles) and for bulk samples via ellipsometry by Munkhbat et al. [74] (diamonds). The square markers represent our own calculation of the refractive indices using Equation (3) and the corresponding coherent phonon frequencies from Table 1. Our estimated value for WSSe shows strong agreement with the bulk experimental data from Ref. [74], although it is slightly lower than that of WS_2. This difference is consistent with Equation (3), given the lower oscillation frequency observed in WSSe. Nevertheless, the refractive index of WSSe is expected to lie within the limits of the range defined by its parent compounds. It is reasonable that the DFT-derived Young's modulus for an ideal Janus crystal [12] differs from the effective modulus in our experimental WSSe alloy, which may account for the modestly lower refractive index estimated by our measurements.

5 | All-Optical Control of the Coherent Acoustic Oscillation

We record the 2D dynamics by sequentially acquiring a series of one-dimensional pump-probe traces, each incorporating an additional pump pulse precisely delayed relative to the original

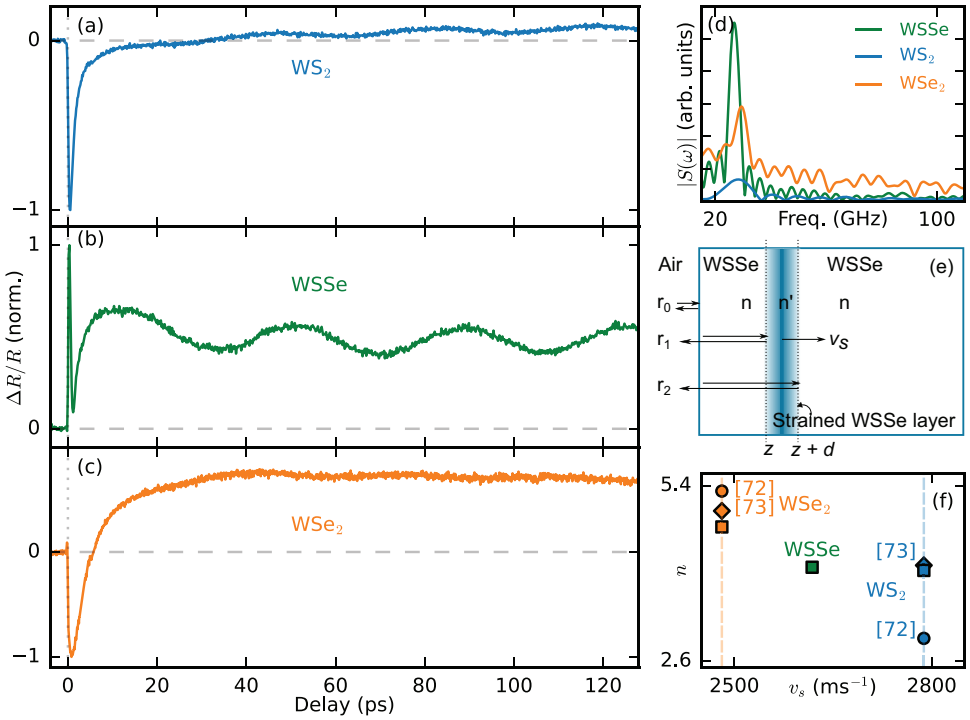

FIGURE 4 | Coherent acoustic phonons in the symmetric parent TMDCs. (a–c) Transient reflection of tungsten-based TMDCs at a fluence of ~ 5 mJ cm^{-2}. While both WS_2 (blue) and WSe_2 (orange) exhibit a similar periodic modulation, their fractional amplitudes are reduced compared to WSSe (green). (d) The Fourier spectrum for each sample peaks at a slightly different frequency. (e) Schematic illustration of a propagating strained WSSe layer. The pump pulse generates a longitudinal coherent acoustic phonon that travels at the speed of sound v_s. The relevant reflection processes in the Fabry-Perot cavity, represented by the arrows, are used to calculate the reflection from the sample. The index of refraction in the strained layer, n', is perturbed with respect to the rest of the sample. (f) Comparison of refractive indices and speed of sound in WS_2 (blue), WSSe (green), and WSe_2 (orange). Different markers denote literature values together with our own, as described in the main text.

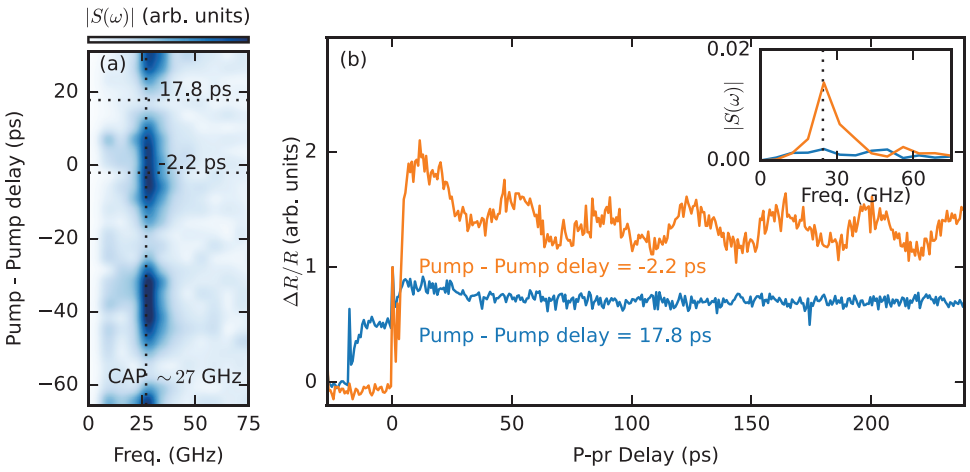

FIGURE 5 | All-optical control of CAPs in WSSe. (a) 2D map of frequency vs. pump-pump delay dynamics. (b) Time domain dynamics for in-phase and out-of-phase excitation with pump pulses of similar fluence. The selected values for pump–pump delays are highlighted in the 2D map with black dotted lines. The curves are normalized to the initial peak of the static pump. For out-of-phase pump pulses (blue) the periodic modulation is completely quenched while the in-phase (orange) excitation shows an increased modulation. Inset: the comparison between Fourier spectra in both cases shows that the peak of the out-of-phase excitation has decreased below the noise level.

excitation using a mechanical delay stage. The second time axis corresponds to the delay introduced by the second pump pulse. The fluence of both pump pulses is F ~ 5 mJ cm^{-2}, ensuring that they generate coherent acoustic oscillations of comparable amplitude. Figure 5a presents a 2D map of frequency versus pump–pump (P-P) delay. In our experimental convention, a negative pump-pump delay indicates that the second pump pulse trails the first, whereas a positive delay indicates that it leads the first. For example, a delay of -2.2 ps corresponds to a trailing second pump pulse, while a delay of 17.8 ps corresponds

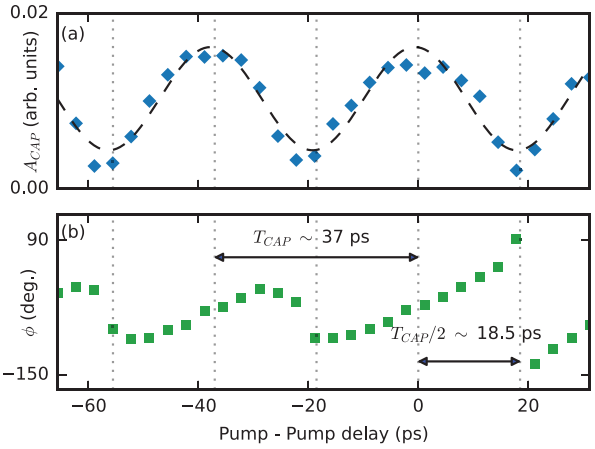

FIGURE 6 | All-optical control of CAPs in WSSe. (a) Complete P-P delay dependence of the phonon peak. The amplitude varies as a cosine of the modulation frequency, which represents constructive and destructive interference between coherent acoustic phonon wavepackets. (b) P-P delay dependence of the Fourier phase. Abrupt changes might indicate a back-reflected strain pulse.

to a leading second pump pulse. In the 2D map, the CAP at 27 GHz is highlighted by a vertical black dotted line, together with two horizontal line cuts (highlighted again by black dotted lines) at these representative delays. Figure 5b shows the time-domain transient reflection signals ($\Delta R/R$) for the corresponding pump pulse sequences, normalized to the fast exciton peak of the original pump pulse (at zero delay). The orange curve, recorded at a pump-pump delay of -2.2 ps, exhibits an enhanced oscillatory component, indicating that the CAP wavepackets generated by the two pump pulses constructively interfere. In contrast, the blue curve, obtained at a pump-pump delay of 17.8 ps, shows the characteristic recovery of the transient reflectivity after photoexcitation attributed to the PR mechanism, but a complete suppression of the periodic modulation, evidence of a destructive interference effect between the coherent phonon wavepackets. The inset, which displays the corresponding spectral magnitude of both time-domain traces, further confirms that the CAP is quenched under out-of-phase photoexcitation.

A general rule is that when the pump–pump delay $\simeq (2n + 1)T_{CAP}/2$, the CAPs interfere destructively, whereas delays near an integer multiple of $T_{CAP} = 37$ ps lead to constructive interference. This behavior is illustrated in Figure 6a, where the magnitude of the CAP at 27 GHz is plotted as a function of the delay between pump pulses, following the black vertical line highlighted in Figure 6a. The experimental data (blue diamonds) follows a periodic function described by $\cos(2\pi f t + \varphi)$, as shown by the black dashed line. In our analysis, we set the phase constant φ to zero, assuming that at zero pump–pump delay the pulses are perfectly in phase, yielding maximal constructive interference and the highest oscillation amplitude.

Figure 6b depicts the spectral phase as a function of the pump-pump delay, with vertical dotted lines provided as guides. Starting from complete destructive interference at a pump-pump delay of -18.5 ps, the phase of the oscillating signal exhibits an approximately linear dependence on the delay. After one period—at a pump–pump delay of 18.5 ps—the phase exhibits an abrupt jump of $\Delta\phi = 245°$. This phase jump recurs each time the amplitude reaches a minimum due to destructive interference. A similar phenomenon has been observed in InGaN/GaN quantum well structures [75], where the shift is attributed to a reversal of the propagation direction of the acoustic wave. Further investigation, however, is needed to fully understand this behavior in bulk WSSe, where the crystal is assumed to be effectively infinite along the propagation direction.

In conclusion, we have used single- and double-pump transient-reflection spectroscopy to resolve the ultrafast evolution of the photoinduced electronic and lattice degrees of freedom in bulk-like WSSe flakes under high-fluence, above-band excitation. The data reveal a hierarchy of carrier-lattice processes with distinct temporal signatures. At early delays, the transient signal exhibits a rapid exponential decay that reflects fast carrier thermalization, nonradiative trapping, and exciton formation, consistent with excitation into the high-energy D-exciton absorption band, which is expected to persist in few-layer and bulk TMDCs. This is followed by a recovery of the reflectivity on a sub-picosecond timescale (~950 fs), which we attribute to repopulation of conduction band states via a phonon recycling mechanism. At later delays, a coherent acoustic phonon emerges, generated predominantly through the deformation potential mechanism and further strengthened by thermoelastic contributions at high fluence. The fractional amplitude and persistence of this oscillatory component are markedly larger in WSSe than in the binary endpoint crystals WS_2 and WSe_2. Such an enhancement is compatible with the presence of a weak, out-of-plane dipole field in the alloy arising from its chalcogen asymmetry, although additional measurements will be required to confirm its role in bulk-like samples.

Using a two-pulse excitation scheme, we also demonstrated all-optical control of the CAP dynamics: by adjusting the interpulse delay relative to the phonon period, we achieved destructive interference for out-of-phase excitation and constructive enhancement for in-phase excitation. The cosine-like modulation of the CAP amplitude with pump-pump delay provides a clear signature of interference between independently launched coherent wavepackets.

These results highlight the unique opportunities offered by asymmetric TMDC alloys for tailoring ultrafast optomechanical responses and suggest new routes toward high-performance actuators and nanoresonators based on layered chalcogenide materials. This work also motivates further investigation into the synthesis and characterization of ideal Janus materials for future hybrid photonic applications, where stronger, uniform structural asymmetries may offer even greater tunability and control of coherent lattice dynamics.

Author Contributions

Sergio I. Rey: conceptualization (lead); data curation (lead); formal analysis (lead); investigation (lead); methodology – setup design and sample preparation (lead); validation (equal); visualization (lead); writing – original draft (lead); writing – review and editing (equal). **Martin J. Cross**: data curation (supporting); methodology (supporting); validation

(equal); writing – review and editing (supporting). **Malte L. Welsch**: data curation (supporting); methodology (supporting); validation (equal); writing – review and editing (supporting). **Frederik Schröder**: methodology – sample preparation (equal); validation (equal); writing – review and editing (equal). **William Carstensen**: methodology (supporting); validation (supporting); writing – review and editing (supporting). **Oleg Semenov**: methodology – Raman Spectroscopy (lead); validation (equal); writing – review and editing (equal). **Daphne M. Dekker**: methodology – X–ray diffraction (lead); validation (equal); writing – review and editing (equal). **Nikolai K. Orlov**: methodology – EBSD and EDX data (lead); validation (equal); writing – review and editing (equal). **Binbin Zhou**: methodology (supporting); supervision (equal); validation (equal); writing – review and editing (equal). **Nicolas Stenger**: conceptualization (equal); methodology – sample preparation (supporting); validation (equal); writing – review and editing (equal). **Peter U. Jepsen**: funding acquisition (equal); investigation (equal); methodology (equal); resources (equal); supervision (equal); validation (equal); writing – review and editing (equal). **Edmund J. R. Kelleher**: conceptualization (equal); funding acquisition (lead); investigation (equal); methodology (equal); resources (lead); supervision (lead); validation (equal); writing – review and editing (lead).

Acknowledgments

S.I.R. and E.J.R.K. acknowledge financial support from the Independent Research Fund Denmark Sapere Aude grant (project number 9064-00072B). F.S. and N.S. acknowledge support from the Danish National Research Foundation through NanoPhoton–Center for Nanophotonics (grant number DNRF147). N.S. acknowledges funding by the Novo Nordisk Foundation NERD Programme (project QuDec NNF23OC0082957). S.I.R. acknowledges financial support from the European Union's Horizon Research and Innovation program under grant agreement No. 101017720 (FET-Proactive EBEAM). O.S. acknowledges financial support from HORIZON EIC Pathfinder project ReaCtor (No. 101099405). D.D. acknowledges financial support from the Dutch Research Council (NWO) project no. KICH1.ED02.20.007. N.O. acknowledges support from the Dutch Research Council (NWO), Gatan (EDAX), Amsterdam Scientific Instruments (ASI) an CL solutions under project "Achieving Semiconductor Stability From The Ground Up" (No. 19459).

Conflicts of Interest

The authors declare no conflicts of interest.

Data Availability Statement

The data that support the findings of this study are available from the corresponding author upon reasonable request.

References

1. C. Lee, X. Wei, J. W. Kysar, and J. Hone, "Measurement of the Elastic Properties and Intrinsic Strength of Monolayer Graphene," *Science* 321, no. 5887 (2008): 385–388.

2. A. A. Balandin, S. Ghosh, W. Bao, et al., "Superior Thermal Conductivity of Single-Layer Graphene," *Nano Letters* 8, no. 3 (2008): 902–907.

3. K. I. Bolotin, K. J. Sikes, Z. Jiang, et al., "Ultrahigh Electron Mobility in Suspended Graphene," *Solid State Communications* 146, no. 9 (2008): 351–355.

4. L. Song, L. Ci, H. Lu, et al., "Large-Scale Growth and Characterization of Atomic Hexagonal Boron Nitride Layers," *Nano Letters* 10, no. 8 (2010): 3209–3215.

5. A. A. Soluyanov, D. Gresch, Z. Wang, et al., "Type-II Weyl Semimetals," *Nature* 527, no. 7579 (2015): 495–498.

6. H. Zhang, C.-X. Liu, X.-L. Qi, X. Dai, Z. Fang, and S.-C. Zhang, "Topological Insulators in Bi_2Se_3, Bi_2Te_3, and Sb_2Te_3 with a Single Dirac Cone on the Surface," *Nature Physics* 5, no. 6 (2009): 438–442.

7. M. S. El-Bana, D. Wolverson, S. Russo, G. Balakrishnan, D. M. Paul, and S. J. Bending, "Superconductivity in Two-Dimensional $NbSe_2$ Field-Effect Transistors," *Superconductor Science and Technology* 26, no. 12 (2013): 125020.

8. K. F. Mak, C. Lee, J. Hone, J. Shan, and T. F. Heinz, "Atomically Thin MoS_2: A New Direct-Gap Semiconductor," *Physical Review Letters* 105, no. 13 (2010): 136805.

9. A. Splendiani, L. Sun, Y. Zhang, et al., "Emerging Photoluminescence in Monolayer MoS_2," *Nano Letters* 10, no. 4 (2010): 1271–1275.

10. D. Xiao, G.-B. Liu, W. Feng, X. Xu, and W. Yao, "Coupled Spin and Valley Physics in Monolayers of MoS_2 and Other Group-VI Dichalcogenides," *Physical Review Letters* 108, no. 19 (2012): 196802.

11. X. Xu, W. Yao, D. Xiao, and T. F. Heinz, "Spin and Pseudospins in Layered Transition Metal Dichalcogenides," *Nature Physics* 10, no. 5 (2014): 343–350.

12. L. Dong, J. Lou, and V. B. Shenoy, "Large In-Plane and Vertical Piezoelectricity in Janus Transition Metal Dichalcogenides," *ACS Nano* 11, no. 8 (2017): 8242–8248.

13. T. Zheng, Y.-C. Lin, Y. Yu, et al., "Excitonic Dynamics in Janus MoSSe and WSSe Monolayers," *Nano Letters* 21, no. 2 (2021): 931–937.

14. C. W. Jang, W. J. Lee, J. K. Kim, S. M. Park, S. Kim, and S.-H. Choi, "Growth of Two-Dimensional Janus MoSSe by a Single In Situ Process without Initial or Follow-Up Treatments," *NPG Asia Materials* 14, no. 1 (2022): 1–8.

15. A.-Y. Lu, H. Zhu, J. Xiao, et al., "Janus Monolayers of Transition Metal Dichalcogenides," *Nature Nanotechnology* 12, no. 8 (2017): 744–749.

16. K. O. Pucko, E. Blundo, N. Zawadzka, et al., "Excitons and Trions in WSSe Monolayers," *2D Materials* 10, no. 1 (2022): 015018.

17. S. Chakraborty and S. Raj, "Anisotropic Rashba Effect in Two-Dimensional Non-Janus Transition-Metal Dichalcogenide MSSe(M = Mo, W) Alloys," *Physical Review B* 107, no. 3 (2023): 035420.

18. S. Wall, D. Wegkamp, L. Foglia, et al., "Ultrafast Changes in Lattice Symmetry Probed by Coherent Phonons," *Nature Communications* 3, no. 1 (2012): 721.

19. M. Borsch, M. Meierhofer, R. Huber, and M. Kira, "Lightwave Electronics in Condensed Matter," *Nature Reviews Materials* 8, no. 10 (2023): 668–687.

20. D. M. Moss, A. V. Akimov, B. A. Glavin, M. Henini, and A. J. Kent, "Ultrafast Strain-Induced Current in a GaAs Schottky Diode," *Physical Review Letters* 106, no. 6 (2011): 066602.

21. K. O'Brien, N. D. Lanzillotti-Kimura, J. Rho, H. Suchowski, X. Yin, and X. Zhang, "Ultrafast Acousto-Plasmonic Control and Sensing in Complex Nanostructures," *Nature Communications* 5, no. 1 (2014): 4042.

22. J.-W. Kim, M. Vomir, and J.-Y. Bigot, "Ultrafast Magnetoacoustics in Nickel Films," *Physical Review Letters* 109, no. 16 (2012): 166601.

23. C. Thomsen, J. Strait, Z. Vardeny, H. J. Maris, J. Tauc, and J. J. Hauser, "Coherent Phonon Generation and Detection by Picosecond Light Pulses," *Physical Review Letters* 53, no. 10 (1984): 989–992.

24. C. Thomsen, H. T. Grahn, H. J. Maris, and J. Tauc, "Surface Generation and Detection of Phonons by Picosecond Light Pulses," *Physical Review B* 34, no. 6 (1986): 4129–4138.

25. S. A. Akhmanov and V. É. Gusev, "Laser Excitation of Ultrashort Acoustic Pulses: New Possibilities in Solid-State Spectroscopy, Diagnostics of Fast Processes, and Nonlinear Acoustics," *Soviet Physics Uspekhi* 35, no. 3 (1992): 153.

26. R. Merlin, "Generating Coherent THz Phonons with Light Pulses," *Solid State Communications* 102, no. 2 (1997): 207–220.

27. S. Ge, X. Liu, X. Qiao, et al., "Coherent Longitudinal Acoustic Phonon Approaching THz Frequency in Multilayer Molybdenum Disulfide," *Scientific Reports* 4, no. 1 (2014): 5722.

28. X. Chen, S. Zhang, L. Wang, et al., "Direct Observation of Interlayer Coherent Acoustic Phonon Dynamics in Bilayer and Few-Layer $PtSe_2$," *Photonics Research* 7, no. 12 (2019): 1416–1424.

29. C.-F. Huo, R. Wen, X.-Q. Yan, et al., "Thickness-Dependent Ultrafast Charge-Carrier Dynamics and Coherent Acoustic Phonon Oscillations in Mechanically Exfoliated $PdSe_2$ Flakes," *Physical Chemistry Chemical Physics* 23, no. 36 (2021): 20666–20674.

30. J. D. G. Greener, A. V. Akimov, V. E. Gusev, et al., "Coherent Acoustic Phonons in van der Waals Nanolayers and Heterostructures," *Physical Review B* 98, no. 7 (2018): 075408.

31. T. G. Park, H. R. Na, S.-H. Chun, W. B. Cho, S. Lee, and F. Rotermund, "Coherent Control of Interlayer Vibrations in Bi_2Se_3 van der Waals Thin Films," *Nanoscale* 13, no. 45 (2021): 19264–19273.

32. T. G. Park, S. Baek, J. Park, et al., "Ultrafast Switching of Topological Invariants by Light-Driven Strain," in CLEO 2023, Technical Digest Series (Optica Publishing Group), (2023): paper FF2G.2.

33. C. Nayak, S. Masanta, S. Ghosh, et al., "Valley Polarization and Photocurrent Generation in Transition Metal Dichalcogenide Alloy $MoS_{2x}Se_{2(1-x)}$," *Physical Review B* 109 (2024): 115304.

34. P. Valencia-Acuna, P. Zereshki, M. M. Tavakoli, J.-H. Park, J. Kong, and H. Zhao, "Transient Absorption of Transition Metal Dichalcogenide Monolayers Studied by a Photodope-Pump-Probe Technique," *Physical Review B* 102, no. 3 (2020): 035414.

35. P. D. Cunningham, A. T. Hanbicki, K. M. McCreary, and B. T. Jonker, "Photoinduced Bandgap Renormalization and Exciton Binding Energy Reduction in WS_2," *ACS Nano* 11, no. 12 (2017): 12601–12608.

36. N. Vashistha, M. Kumar, R. K. Singh, D. Panda, L. Tyagi, and S. Chakrabarti, "A Comprehensive Study of Ultrafast Carrier Dynamics of LT-GaAs: Above and Below Bandgap Regions," *Physica B: Condensed Matter* 602 (2021): 412441.

37. X. Wang, G. Niu, J. Jiang, et al., "Anomalous Dynamics of Defect-Assisted Phonon Recycling in Few-Layer $Mo_{0.5}W_{0.5}S_2$," *The Journal of Physical Chemistry Letters* 13, no. 44 (2022): 10395–10403.

38. F. Ceballos, Q. Cui, M. Z. Bellus, and H. Zhao, "Exciton Formation in Monolayer Transition Metal Dichalcogenides," *Nanoscale* 8, no. 22 (2016): 11681–11688.

39. X.-C. Nie, H.-Y. Liu, X. Zhang, et al., "Exciton-Phonon and Exciton-Exciton Interactions in GaAs by Time-Resolved Optical Reflectivity," *Results in Physics* 12 (2019): 1089–1090.

40. X.-C. Nie, H.-Y. Song, F. Li, et al., "Transient Carrier Dynamics of GaAs at Room Temperature," *Journal of Applied Physics* 128, no. 1 (2020): 015706.

41. C. Trovatello, F. Katsch, N. J. Borys, et al., "The Ultrafast Onset of Exciton Formation in 2D Semiconductors," *Nature Communications* 11, no. 1 (2020): 5277.

42. K. Wei, Y. Sui, Z. Xu, et al., "Acoustic Phonon Recycling for Photocarrier Generation in Graphene-WS_2 Heterostructures," *Nature Communications* 11, no. 1 (2020): 3876.

43. D. Soranzio, M. Peressi, R. J. Cava, F. Parmigiani, and F. Cilento, "Ultrafast Broadband Optical Spectroscopy for Quantifying Subpicometric Coherent Atomic Displacements in WTe_2," *Physical Review Research* 1, no. 3 (2019): 032033.

44. Y. Xiao, N. A. Charipar, J. Salman, A. Piqué, and M. A. Kats, "Nanosecond Mid-Infrared Pulse Generation via Modulated Thermal Emissivity," *Light: Science & Applications* 8, no. 1 (2019): 51.

45. Z. Chi, H. Chen, Q. Zhao, and Y.-X. Weng, "Observation of the Hot-Phonon Effect in Monolayer MoS_2," *Nanotechnology* 31, no. 23 (2020): 235712.

46. J. Wagner, H. Kuhn, R. Bernhardt, J. Zhu, and P. H. M. van Loosdrecht, "Trap-Induced Long Exciton Intervalley Scattering and Population Lifetime in Monolayer WSe_2," *2D Materials* 8, no. 3 (2021): 035018.

47. Q. Liu, K. Wei, Y. Tang, Z. Xu, X. Cheng, and T. Jiang, "Visualizing Hot-Carrier Expansion and Cascaded Transport in WS_2 by Ultrafast Transient Absorption Microscopy," *Advanced Science* 9, no. 10 (2022): 2105746.

48. P. Adhikari, P. Wang, K. Kobbekaduwa, et al., "Generating and Capturing Secondary Hot Carriers in Monolayer Tungsten Dichalcogenides," *The Journal of Physical Chemistry Letters* 13, no. 25 (2022): 5703–5710.

49. P. Ruello and V. E. Gusev, "Physical Mechanisms of Coherent Acoustic Phonon Generation by Ultrafast Laser Action," *Ultrasonics* 56 (2015): 21–35.

50. O. Matsuda, O. B. Wright, D. H. Hurley, V. E. Gusev, and K. Shimizu, "Coherent Shear Phonon Generation and Detection with Ultrashort Optical Pulses," *Physical Review Letters* 93, no. 9 (2004): 095501.

51. E. S. K. Young, A. V. Akimov, R. P. Campion, A. J. Kent, and V. Gusev, "Picosecond Strain Pulses Generated by a Supersonically Expanding Electron-Hole Plasma in GaAs," *Physical Review B* 86, no. 15 (2012): 155207.

52. X.-R. Ma, Y.-C. Li, C. Ge, P. Wang, H.-Y. Song, and S.-B. Liu, "Ultrafast Generation and Detection of Coherent Acoustic Phonons in $SnS_{0.91}Se_{0.09}$," *Results in Physics* 45 (2023): 106241.

53. Priya, E. R. Cardozo de Oliveira, and N. D. Lanzillotti-Kimura, "Perspectives on High-Frequency Nanomechanics, Nanoacoustics, and Nanophononics," *Applied Physics Letters* 122, no. 14 (2023): 140501.

54. A. K. Prasad, J. Šebesta, R. Esteban-Puyuelo, et al., "Nonequilibrium Phonon Dynamics and Its Impact on the Thermal Conductivity of the Benchmark Thermoelectric Material SnSe," *ACS Nano* 17, no. 21 (2023): 21006–21017.

55. Z. Chi, H. Chen, Q. Zhao, and Y.-X. Weng, "Ultrafast Carrier and Phonon Dynamics in Few-Layer 2H – $MoTe_2$," *The Journal of Chemical Physics* 151, no. 11 (2019): 114704.

56. T. Fukuda, K. Makino, Y. Saito, et al., "Coherent Optical Response Driven by Non-Equilibrium Electron–Phonon Dynamics in a Layered Transition-Metal Dichalcogenide," *APL Materials* (2024).

57. A. Chernikov, C. Ruppert, H. M. Hill, A. F. Rigosi, and T. F. Heinz, "Population Inversion and Giant Bandgap Renormalization in Atomically Thin WS_2 Layers," *Nature Photonics* 9, no. 7 (2015): 466–470.

58. K. K. Kam and B. A. Parkinson, "Detailed Photocurrent Spectroscopy of the Semiconducting Group VIB Transition Metal Dichalcogenides," *The Journal of Physical Chemistry* 86, no. 4 (1982): 463–467.

59. J. Gusakova, X. Wang, L. L. Shiau, et al., "Electronic Properties of Bulk and Monolayer TMDs: Theoretical Study within the DFT Framework (GVJ-2e Method)," *Physica Status Solidi A* 214, no. 12 (2017): 1700218.

60. G. Gautschi, *Piezoelectric Sensorics* (Springer, 2002).

61. J.-W. Yeh, S.-K. Chen, S.-J. Lin, et al., "Nanostructured High-Entropy Alloys with Multiple Principal Elements: Novel Alloy Design Concepts and Outcomes," *Advanced Engineering Materials* 6, no. 5 (2004): 299–303.

62. Y.-W. Chen, J.-J. Ruan, J.-M. Ting, Y.-H. Su, and K.-S. Chang, "Solution-Based Fabrication of High-Entropy $Ba(Ti, Hf, Zr, Fe, Sn)O_3$ Films on Fluorine-Doped Tin Oxide Substrates and Their Piezoelectric Responses," *Ceramics International* 47, no. 8 (2021): 11451–11458.

63. F. Tasnádi, B. Alling, C. Höglund, et al., "Origin of the Anomalous Piezoelectric Response in Wurtzite $Sc_xAl_{1-x}N$ Alloys," *Physical Review Letters* 104, no. 13 (2010): 137601.

64. K. R. Talley, S. L. Millican, J. Mangum, et al., "Implications of Heterostructural Alloying for Enhanced Piezoelectric Performance of (Al,Sc)N," *Physical Review Materials* 2, no. 6 (2018): 063802.

65. Y. Chen, Z. Tian, X. Wang, et al., "2D Transition Metal Dichalcogenide with Increased Entropy for Piezoelectric Electronics," *Advanced Materials* 34, no. 48 (2022): 2201630.

66. C. Yu, X. Chen, C. Wang, and Z. Wang, "Mechanical Elasticity and Piezoelectricity in Monolayer Transition-Metal Dichalcogenide Alloys," *Journal of Physics and Chemistry of Solids* 135 (2019): 109081.

67. V. J. Gokhale and M. Rais-Zadeh, "Phonon-Electron Interactions in Piezoelectric Semiconductor Bulk Acoustic Wave Resonators," *Scientific Reports* 4, no. 1 (2014): 5617.

68. R. Liu, G. D. Sanders, C. J. Stanton, et al., "Femtosecond Pump-Probe Spectroscopy of Propagating Coherent Acoustic Phonons in $In_xGa_{1-x}N$/GaN Heterostructures," *Physical Review B* 72, no. 19 (2005): 195335.

69. M. Cardona, "Modulation Spectroscopy of Semiconductors," in *Festkörperprobleme 10: Advances in Solid State Physics*, ed. O. Madelung (Springer, 1970), 125–173.

70. M. Eagleson, *Concise Encyclopedia of Chemistry* (De Gruyter, 2011).

71. M. K. Agarwal and P. A. Wani, "Growth Conditions and Crystal Structure Parameters of Layer Compounds in the Series $Mo_{1-x}W_xSe_2$," *Materials Research Bulletin* 14, no. 6 (1979): 825–830.

72. C. Muratore, V. Varshney, J. J. Gengler, et al., "Cross-Plane Thermal Properties of Transition Metal Dichalcogenides," *Applied Physics Letters* 102, no. 8 (2013): 081604.

73. C. Hsu, R. Frisenda, R. Schmidt, et al., "Thickness-Dependent Refractive Index of 1L, 2L, and 3L MoS_2, $MoSe_2$, WS_2, and WSe_2," *Advanced Optical Materials* 7, no. 13 (2019): 1900239.

74. B. Munkhbat, P. Wróbel, T. J. Antosiewicz, and T. O. Shegai, "Optical Constants of Several Multilayer Transition Metal Dichalcogenides Measured by Spectroscopic Ellipsometry in the 300–1700 nm Range: High Index, Anisotropy, and Hyperbolicity," *ACS Photonics* 9, no. 7 (2022): 2398–2407.

75. C.-K. Sun, Y.-K. Huang, J.-C. Liang, A. Abare, and S. P. DenBaars, "Coherent Optical Control of Acoustic Phonon Oscillations in InGaN/GaN Multiple Quantum Wells," *Applied Physics Letters* 78, no. 9 (2001): 1201–1203.

Supporting Information

Additional supporting information can be found online in the Supporting Information section.

Supporting File: apxr70102-sup-0001-SuppMat.docx.